Journal Pre-proof

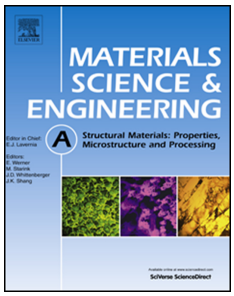

Additive manufacturing of TiB_2-containing CoCrFeMnNi high-entropy alloy matrix composites with high density and enhanced mechanical properties

Y.L. Wang, L. Zhao, D. Wan, S. Guan, K.C. Chan

PII: S0921-5093(21)01137-0

DOI: https://doi.org/10.1016/j.msea.2021.141871

Reference: MSA 141871

To appear in: *Materials Science & Engineering A*

Received Date: 16 March 2021

Revised Date: 3 August 2021

Accepted Date: 5 August 2021

Please cite this article as: Y.L. Wang, L. Zhao, D. Wan, S. Guan, K.C. Chan, Additive manufacturing of TiB_2-containing CoCrFeMnNi high-entropy alloy matrix composites with high density and enhanced mechanical properties, *Materials Science & Engineering A* (2021), doi: https://doi.org/10.1016/j.msea.2021.141871.

CRediT author statement

Wang, Yilin: Conceptualization, Methodology, Data curation, Writing - original draft, Writing - review & editing. **Zhao, lei**: Writing - review & editing. **Wan, Di**: Data curation, Writing - review & editing. **Guan, Shuai**: Writing - review & editing. **K.C. Chan**: Supervision, Conceptualization, Writing - review & editing.

Additive manufacturing of TiB_2-containing CoCrFeMnNi high-entropy alloy matrix composites with high density and enhanced mechanical properties

Y.L. Wang[a], L. Zhao[a], D. Wan[b], S, Guan[a], K.C. Chan[a,] *

a. Advanced Manufacturing Technology Research Centre, Department of Industrial and Systems Engineering, The Hong Kong Polytechnic University, Hung Hom, Kowloon, Hong Kong

b. Department of Mechanical and Industrial Engineering, Norwegian University of Science and Technology, Richard Birkelands vei 2B, 7491 Trondheim, Norway

∗ Corresponding author. E-mail address: kc.chan@polyu.edu.hk (K.C. Chan).

Abstract

Near-fully dense CoCrFeMnNi high-entropy alloy (HEA) matrix composites reinforced with 5 wt% TiB_2 nanoparticles were successfully additively manufactured via the laser-engineered net shaping technique. Compared to the monolithic CoCrFeMnNi printing process, a higher energy density input is shown to produce a synergic combination of Marangoni flow and capillary force in the laser-generated melt pool. It facilitates the enhancement of wettability, and hence a more uniform distribution of the reinforcement material and a high degree of densification of 99.72%, which are able to delay the early fracture of the material. The as-deposited composites exhibit improved yield strength, surpassing that of the monolithic HEA by 42%. The enhanced strength is mainly ascribed to dispersion strengthening. Besides, the refined grain size, the increased dislocation density, and the additional load transfer effect also

contribute to the strength enhancement. Furthermore, the wear resistance properties of the CoCrFeMnNi/TiB_2 composite are also shown to be superior to those of the CoCrFeMnNi, indicating a decrease in friction coefficient by 22.4%. The enhanced tribological properties are attributed to the synergic effect of high-hardness and self-lubrication of TiB_2 nanoparticles. The findings provide guidelines for achieving high-performance HEA-matrix composites.

Keywords: High-entropy alloy; Additive manufacturing; Metal matrix composite; Mechanical property

1. Introduction

The high-entropy alloys (HEAs) concept has opened up a new avenue for alloy design in the metallurgical research area [1], which encompasses broad-spectrum microstructures and properties. In recent years, a large majority of HEAs have been developed, and CoCrFeMnNi HEA with a single face-centered cubic (FCC) structure has received considerable attention in terms of its extraordinary fracture toughness and exceptional ductility, especially at cryogenic temperatures [2, 3]. Nevertheless, the insufficient strength and wear resistance of the CoCrFeMnNi HEA preclude its widespread applications as structural materials [3, 4].

Metal matrix composites (MMCs), introducing high-stiffness second phase dispersions into the soft matrix, possess superior strength and excellent tribology performance. Traditional consolidation techniques within the community of MMCs include high-pressure diffusion bonding [5], powder metallurgy [6], and hot pressing [7], etc. However, these techniques still have unresolved issues associated with the high agglomeration tendency of nano-reinforcements, and hence a high propensity for microstructural inhomogeneity and reduced wettability [7, 8]. Likewise, undesirable grain coarsening observed in conventionally fabricated-MMCs also impairs their mechanical properties [9]. Additive manufacturing (AM), as an emerging technology in fabricating parts in a layer-wise manner, provides a new possibility for fabricating

intricate geometric and high-performance MMCs [10-12]. The super-fast solidification characteristics (cooling rate of 10^3-10^6 K/s) intrinsic to AM facilitate the uniform dispersion of reinforcements and formation of fine-grained microstructures, thus alleviating some of the issues of MMCs produced by conventional methods[13, 14]. In the literature, several attempts have been made to manufacture metallic matrix with different reinforcements via AM, such as TiN/$AlSi_{10}Mg$ nanocomposite [15], TiB_2-reinforced 316L stainless steel [16], and $(FeCrNiCu)_{1-x}$-NbC_x composites [17]. As reported by the aforementioned studies, ceramic reinforcements exhibit significant strengthening capability. However, the degraded densification of the composites induced by ceramic addition may in turn exert a limitation to the mechanical improvement of the AM-ed MMCs. This is in line with the fact that the coexistence of solid particles in the melt pool reduces the dynamic viscosity, thereby weakening the overall rheological property of the solidification front [18]. The suppressed fluidity is believed to be one of the main causes leading to the balling effect and gas pore formation in the metal printing process [19, 20]. Xi et al. [21] demonstrated that a low porosity percentage (~1%) of TiB_2 reinforced Al-based composites could only be obtained at a low reinforcement content of 1 wt%. Further addition of ceramic particles to 5 wt% introduced negative effects on both tensile strength and ductility due to the promoted formation of defects. Abolhasani et al. [18] prepared eutectic Al_2O_3-ZrO_2 reinforced AISI 304 via selective laser melting (SLM), which was capable of a 200% enhancement in microhardness. Nevertheless, increasing the content of nanoparticles deteriorated the density of the composite, resulting in a low relative density of 97.5% with 3 wt% eutectic ceramic mixture addition. Similar arguments hold for *in-situ* nano/submicro-sized carbides reinforced iron by SLM [8], TiC/Inconel 690 composite by direct laser deposition [22], and nano-TiN modified HEA by SLM [23]. Generally, the defects act as stress raisers and undergo abrupt failure during service. The insufficient manufacturing quality hinders the further pursuit of high-performance structural materials. Herein, care must be exercised while applying this strategy.

Achieving a high degree of densification above 99% is an existing challenge within AM fabricated MMCs research community.

TiB_2 exhibits superior thermal stability (melting point: 3243 K) and low density (4.52 g/cm³) and is therefore recognized as an appealing reinforcement for various alloy systems [12, 16, 21]. In this work, near-fully dense 5 wt% TiB_2 nano-particle reinforced CoCrFeMnNi HEA matrix composites are additively manufactured by laser engineered net shaping (LENS). A comprehensive examination of defects and microstructural features of the as-printed composites is carried out. Both the tensile properties and wear resistance ability, together with the corresponding strengthening mechanisms are further investigated. These findings are expected to open a broader processing window for achieving a wide spectrum of mechanical properties for HEAs.

2. Experimental methods

2.1 Powder preparation

The CoCrFeMnNi pre-alloyed particles were prepared using a plasma rotating electrode process (PREP). The HEA particles (45-150 μm in diameter) were further blended with hexagonal prismatic TiB_2 powders (average size of 50 nm) in a planter ball mill. The weight ratio between HEA and TiB_2 powders was 95:5, and the blending time was 3.5 h. A low milling speed of 230 rpm was adopted to maintain the powder sphericity while homogenizing the whole mixture, thereby guaranteeing the LENS process-applicable fluidity. **Fig. 1a and Fig. 1b** show the morphologies of CoCrFeMnNi HEA powder, with and without TiB_2 particles. Indicated by **Fig. 1b**, the accumulated TiB_2 particles adhered to the HEA powder surface after ball milling and the sphericity of the powder was well preserved.

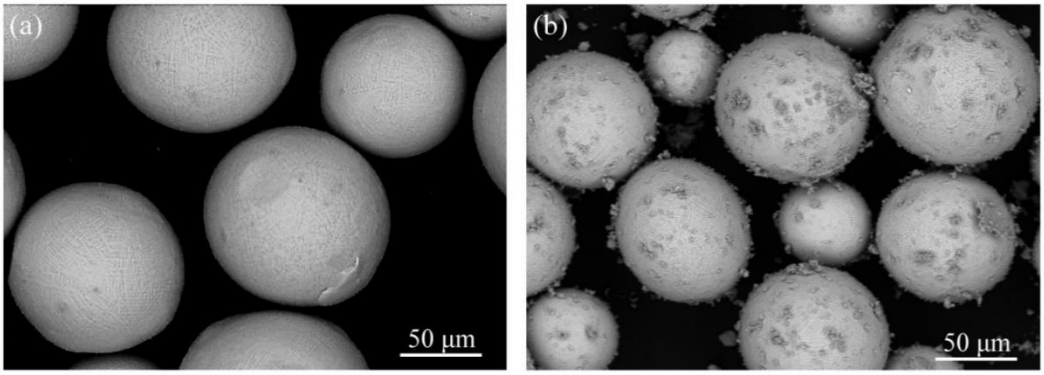

Fig. 1. SEM images of **(a)** CoCrFeMnNi HEA powders and **(b)** CoCrFeMnNi HEA/TiB_2 powders.

2.2 LENS fabrication process

The original CoCrFeMnNi HEA powders and their as-milled mixture were used as the feedstock for LENS (MR7) processing. The LENS technique that adopts a powder feeding system enables rapid solidification by the speedy movement of the coaxial powder feeding laser head, leading to an ultrafast metallurgical process. A laser scanning speed of 5 mm/s, a layer thickness of 300 μm, and a hatching distance of 460 μm were adopted, while different laser powers with an interval of 50 W were used to obtain varied linear energy densities (i.e. the ratio of applied laser energy (W) and scan speed (mm/s)) input and optimize the densification of the as-printed specimens. A bidirectional scan strategy with a rotation of 90° between adjacent layers was used in the printing process. A two-wavelength imaging pyrometer (ThermaViz system), with a high resolution of 12.1 μm/pixel, was used to monitor the thermal behavior of the melt pool during the fabrication process. Real-time temperature thermal imagery data was captured to evaluate the solidification behavior.

2.3 Material characterization

X-ray-Computed tomography (CT) and the Archimedes method were used to quantify the porosity of the as-printed specimens. CT examination (YXLON FF35) was operated at the dual tube mode with a 160 kV transmission X-ray source. The 3D panoramic images for the detection of internal defects were reconstructed via a total of

1200 projections to obtain defect size and spatial distribution. Considering the resolution limits of the CT (3 μm) technique, the Archimedes method was used to accurately characterize the defect level.

The samples were ground up to 2000-grit SiC grinding papers and further electropolished in a perchloric acid (10% vol)-ethanol electrolyte with a voltage of 30 V for 12 s. The phase identification was conducted by X-ray Diffractometer (XRD, Rigaku SmartLab) with a scan speed of 1°/min and a scan range of 40~100°. The as-print microstructures were observed and analyzed with the aid of optical microscopy (OM, Leica), scanning electron microscopy (SEM, Tescan VEGA3) equipped with electron backscatter diffraction (EBSD) and energy dispersive X-ray (EDX) techniques, and transmission electron microscopy (TEM, FEI Talos F200X).

2.4 Mechanical property test and wear test

The as-deposited blocks fabricated by optimized laser parameters were wire-cut and machined into tensile coupons. The gauge dimensions of the rectangular dog-bone-shaped tensile specimens were 7×3×1 mm, with their tensile axis along the direction perpendicular to the printing direction. Room temperature uniaxial tensile tests were performed on an INSTRON 5565 material testing machine with an engineering strain rate of $1 \times 10^{-3}/s$. To ensure the reproducibility of the results, three samples were tested for each condition. Hardness measurements were conducted on an HVS-5 hardness tester with a load of 0.5 kgf and a dwell time of 15 s. Dry sliding tribological tests were performed on a PLINT Tribology TE99 universal wear machine in a ball-on-flat configuration. A Si_3N_4 ball (Φ 6.35 mm) was used as the counterface material against the as-printed specimen. The duration of sliding time for each experiment was 1800 s. The tests were carried out at a constant load of 5 N with an oscillating frequency of 2 Hz and a stroke length of 16 mm. The wear rate (mm^3/Nm) was determined as the ratio of wear volume (mm^3) divided by the product of applied load (N) and sliding distance (m) [24]. SEM was employed to characterize the morphologies of the worn surface. The 3D profiles of the wear surface were measured by offline measurement technology (ZYGO Nexview profiler system).

3. Results and discussion

3.1 Densification characterization and solidification behavior

Based on the criterion of the least defects, the linear energy density input (*P*) was optimized for the achievement of highly dense samples. The relative density was calculated as the ratio of Archimedes method measured density and theoretical density of CoCrFeMnNi/TiB_2 (7.69 g/cm^3) and CoCrFeMnNi HEA (7.98 g/cm^3). **Fig. 2** demonstrates the variation of the relative density with respect to the input linear energy density. It reveals that the degree of densification increases obviously as the elevated energy input and decreases afterwards. The effect of linear energy density input on the densification behavior of the LENS-printed CoCrFeMnNi/TiB_2 composite is similar to that of the monolithic CoCrFeMnNi as shown in **Fig. 2**. In the low energy input region, only relative density below 99% can be achieved for the two compositions. The lack-of-fusion induced pores highly degrade the densification quality, which is attributed to insufficient overall rheological property in the melt pool. Further increasing the linear energy density input has led to the formation of strong particle-particle bonding and the reduction of large-sized imperfections, causing higher densification for both compositions. For the as-deposited CoCrFeMnNi HEA samples, the linear energy inputs of 80 J/mm and 90 J/mm are more appropriated to fabricate specimens with a lower content of defects, leading to a relative density of 99.82% and 99.74%, respectively. Additionally, the CoCrFeMnNi fabricated with 80 J/mm enjoys the refined microstructures which are confirmed by the subsequent EBSD characterization (Section 3.2), and it outperforms the CoCrFeMnNi fabricated with 90 J/mm in the tensile test (Section 3.3). The optimized parameter of the monolithic CoCrFeMnNi is determined to be 80 J/mm. In comparison, a higher linear energy input (90 J/mm) is required for achieving a high density of 99.72% for the CoCrFeMnNi/TiB_2. However, a further increase of the linear energy input has led to a drop of the densification to below 98% with P=110 J/mm for both compositions, due to the overburnt metallic particles and the exacerbated balling effect.

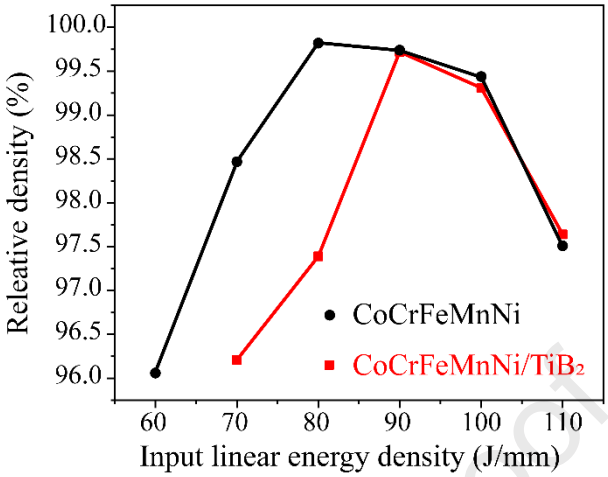

Fig. 2. The variation of the relative density with respect to the input linear energy density.

To further confirm the dense structure of the CoCrFeMnNi/TiB_2 composite fabricated with P=90 J/mm, the reconstructed X-ray CT 3D images are shown in **Fig. 3**. Small cubic regions with a length of 200 μm randomly selected from the 1st, 3rd, 6th, and 10th layers are chosen to evaluate the defects distribution along the printing direction. The results indicate that the pores are relatively distributed randomly throughout the sample, and its average volume fraction is as low as 0.1%. It was slightly lower than the porosity ratio determined by the Archimedes method. The measuring error may arise from the resolution limit of X-ray CT [25]. It is also noteworthy that the extremely large pores, which are commonly reported to deteriorate the deformation response, are not observed. Such a small amount of defects suggests the extremely good printability of the CoCrFeMnNi/TiB_2 composite by additive manufacturing.

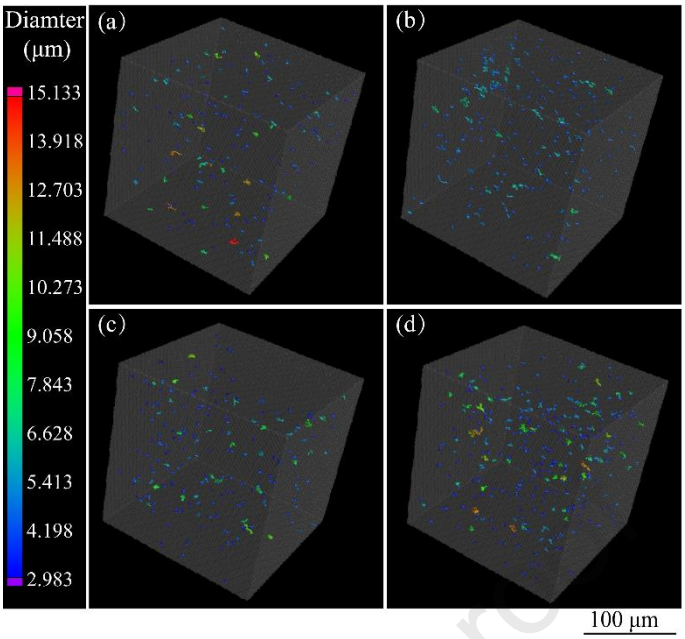

Fig. 3. Defect distributions for the CoCrFeMnNi/TiB_2 composite fabricated with *P*=90 J/mm. **(a-d)** are the corresponding high-resolution 3D X-ray CT micrograph of small regions chosen from the as-deposited **(a)** 1st, **(b)** 3rd, **(c)** 6th, and **(d)** 10th layer, respectively.

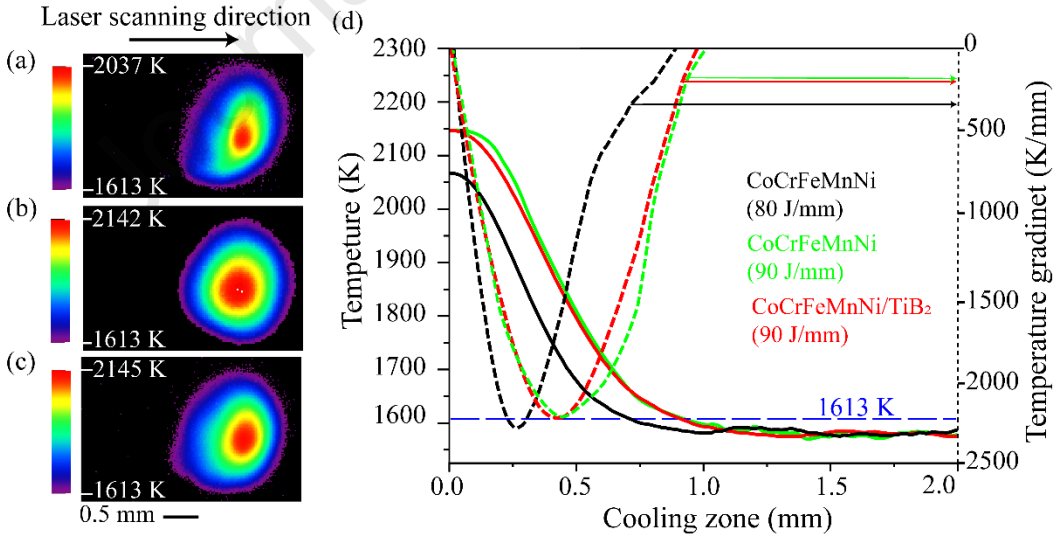

Fig. 4. The thermal maps of melt pool of **(a)** CoCrFeMnNi (80J/mm), **(b)** CoCrFeMnNi (90J/mm) and **(c)** CoCrFeMnNi/TiB_2 (90J/mm); **(d)** Temperature distribution (solid lines) and thermal gradient (dash lines) in the melt pool during

printing. The melting point of CoCrFeMnNi (1613 K) is indicated by the bule broken line in (d).

As discussed above, it is reasonable to believe that the densification behavior of MMCs is affected by the processing conditions. Therefore, it is instructive to examine the solidification behavior for densification optimization. **Fig. 4a-c** show the solidification conditions of the CoCrFeMnNi/TiB_2 composite fabricated with P=90 J/mm as well as the CoCrFeMnNi with both P=80 J/mm and P=90 J/mm. For all these samples, the peak temperature occurred approximately in the central melt pool. Taking the peak temperature as the dividing line, the side of the melt pool opposite to the laser scanning direction is regarded as the cooling zone [26]. The temperature distribution and the thermal gradient in the cooling zone are plotted in **Fig. 4d** to estimate the cooling rate during the laser deposition process.

When comparing the temperature distribution of the melt pool observed under the conditions of P=80 J/mm for CoCrFeMnNi and P=90 J/mm for CoCrFeMnNi with and without TiB_2 addition, a higher linear energy suggests the broadening of melt pool boundary and the increase of peak temperature. The intensified heat accumulation also retards the cooling rate, leading to the largest thermal gradient of the CoCrFeMnNi with P=80 J/mm. Whereas, when the temperature distributions of the two compositions fabricated with the same linear energy density (P=90 J/mm) are compared, there is no obvious difference in the peak temperature as the limited amount of TiB_2 has no significant effect on the instantaneous material-laser interaction. Under the same linear energy input of 90 J/mm, the temperature in the central region of the melt pool of the CoCrFeMnNi specimen is shown to be slightly higher than that of the CoCrFeMnNi/TiB_2 composite. Due to the large difference in thermal conductivity between the two components (CoCrFeMnNi: 12.5 W/m/K [27]; TiB_2:100 W/m/K [28]), the addition of ceramic particles enhances the thermal conductivity of the whole system and accelerates the heat dissipation in the melt pool [22].

The peak temperature during the fabrication of CoCrFeMnNi/TiB_2 composite was about 2145 K, which was much lower than the melting point of TiB_2 (3253 K). It is also consistent with the XRD spectrum for the as-deposited specimen in which there is no interaction between the two components (shown in Section 3.2). The melting point of CoCrFeMnNi (1613 K) [2] was used as a dividing line between the liquids and starting area where solidification occurs, and it is indicated by the blue broken line in **Fig. 4(d).** The thermal gradient (*G*) at the liquid solidification boundary was determined to be 334 K/mm, 196 K/mm and 210 K/mm for CoCrFeMnNi (P=80 J/mm), CoCrFeMnNi (P=90 J/mm) and CoCrFeMnNi/TiB_2 (P=90 J/mm) composite, respectively. The cooling rate (*C*) can be expressed as:

$$C = GS \tag{1}$$

where, *S* represents the solidification rate, which is assumed to be 5 mm/s in this study. Hence, the calculated cooling rate of the laser fabrication process is 1670 K/s (CoCrFeMnNi; P=80 J/mm), 980 K/s (CoCrFeMnNi; P=90 J/mm), and 1050 K/s (CoCrFeMnNi/TiB_2 composite; P=90 J/mm), respectively. It should be noted that the cooling rate of the additive manufacturing process is much higher than the conventional fabrication techniques, in which the cooling speed is generally reported between 200 K/s to 600 K/s. Whatsmore, the addition of TiB_2 particles slightly increases the cooling rate as compared to the monotonic HEA by the same processing parameter, which contributes to the retarding of the grain growth.

During LENS printing, the gradually decayed temperature distribution from the central region of the melt pool to the periphery induces surface tension and spatial flow outward. Benefiting from the intrinsic high cooling speed of additive manufacturing, this kind of speedy Marangoni flow penetrating the solid-liquid interface can serve as the main driving for the rearrangement of particles [29, 30]. As the different thermal physical properties of the metallic matrix and the ceramic reinforcement clusters are an important cause of defects in MMCs, such kind of strong convective activity in the melt pool effectively avoids the formation of large ceramic agglomeration, thus reducing the

defects ratio. Besides, reinforcement addition increases the dynamic viscosity of the solidification system [21], which weakens the rheological properties as well as the wetting characteristics of the melt. That accounts for the reason why the optimized linear energy input for monolithic CoCrFeMnNi (80 J/mm) is insufficient to form highly dense CoCrFeMnNi/TiB_2 composites. With the selected higher energy input for the composites, the viscosity of the melt decreases accordingly. The promoted wettability in solid/liquid interfaces enables the full rearrangement of ceramic particles and effectively alleviates the balling effect, thus forming strong particle-matrix metallurgical bonding [12, 22], and finally enhanced densification. Compared with the monolithic CoCrFeMnNi fabricated with the same high linear energy input (90 J/mm), highly dense samples can be obtained without obvious degradation.

3.2 Microstructural characterization

Fig. 5a presents the SEM image of the as-electropolished CoCrFeMnNi/TiB_2 composites. The sample is free of any visible cracks, despite the presence of a few micro-sized voids. Dispersed TiB_2 particles can be observed in the enlarged SEM images. SEM/EDS mapping (**Fig. 5d-i**) confirms the homogenous elemental distribution. **Fig. 6** shows the XRD patterns of the as-deposited CoCrFeMnNi HEA and CoCrFeMnNi/TiB_2 composite. The CoCrFeMnNi HEA specimen shows a single-phase FCC structure, which is consistent with previous studies [30, 31]. In contrast, additional peaks corresponding to the TiB_2 phases have been identified from the XRD pattern of the as-deposited CoCrFeMnNi/TiB_2 composite.

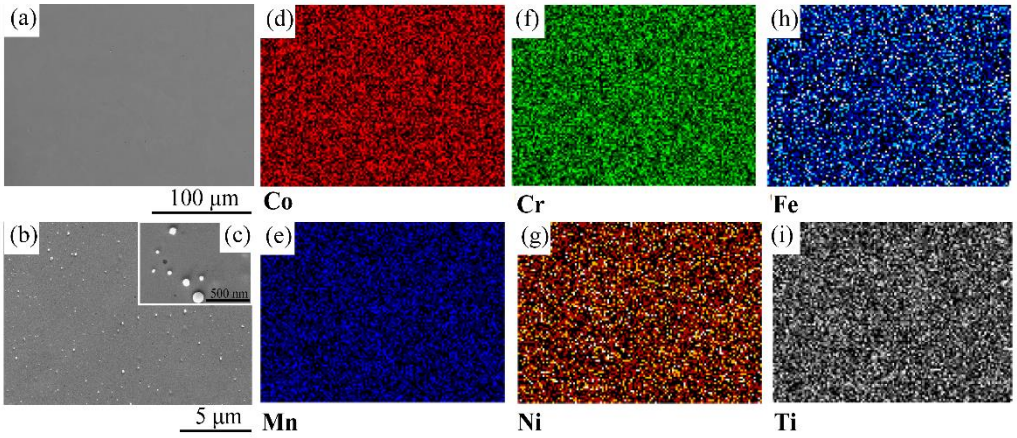

Fig. 5. (a) Low and **(b-c)** high magnification SEM images of the as-printed CoCrFeMnNi/TiB_2 composites; **(d-i)** EDS mapping of the area in (a).

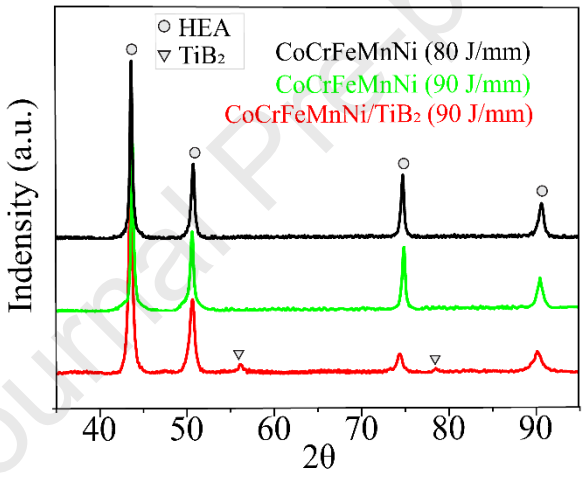

Fig. 6. XRD patterns of the as-deposited CoCrFeMnNi and CoCrFeMnNi/TiB_2 composite.

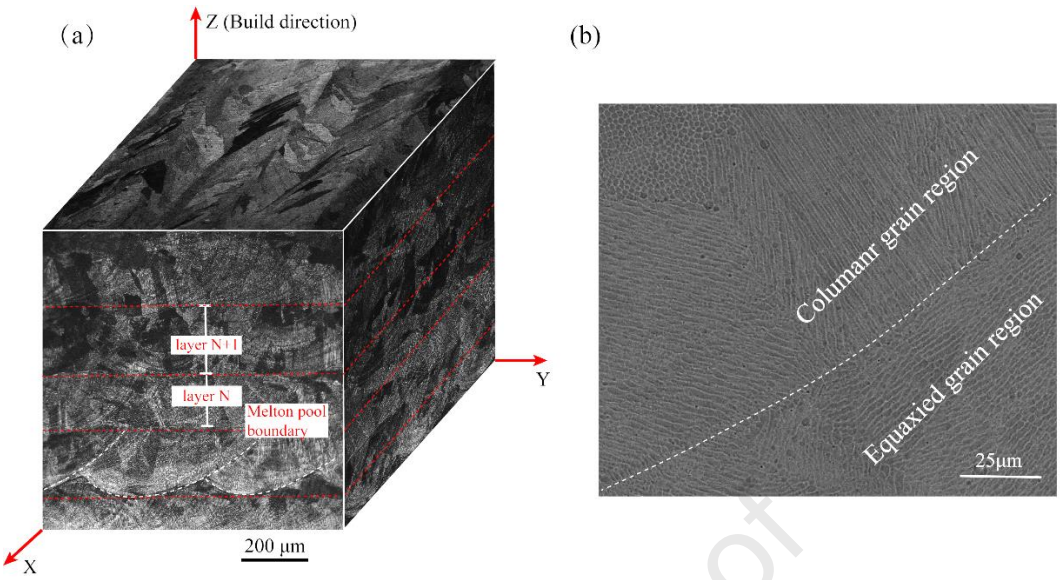

Fig .7. (a) OM and **(b)** SEM images of as-deposited CoCrFeMnNi/TiB_2 composite. The layer boundary and melt pool boundary are highlighted in red and white dashed lines, respectively.

Fig. 7 illustrates the representative optical and SEM images of the etched CoCrFeMnNi/TiB_2 composite. As shown in **Fig.7a,** the LENS fabricated specimen exhibits a laminated pattern. The enlarged SEM micrograph (**Fig .7b**) shows the geometry of the curved melt pool boundary as indicated by the white dash lines. A hierarchical structure could be observed, consisting of cellular epitaxial grown columnar grains dominating in the inner side of the melt pool and cellular structures predominantly existing in the outer side. Moreover, the corresponding optical micrographs of the CoCrFeMnNi fabricate with P=80 J/mm and P=90 J/mm are provided in the Supplementary Information as **Figs. 1**, and the laminated patterns similar to the as-deposited CoCrFeMnNi/TiB_2 composites are observed. Such typical laser-scanning generated features intrinsic to metal printing were also reported in Ref. [2, 15].

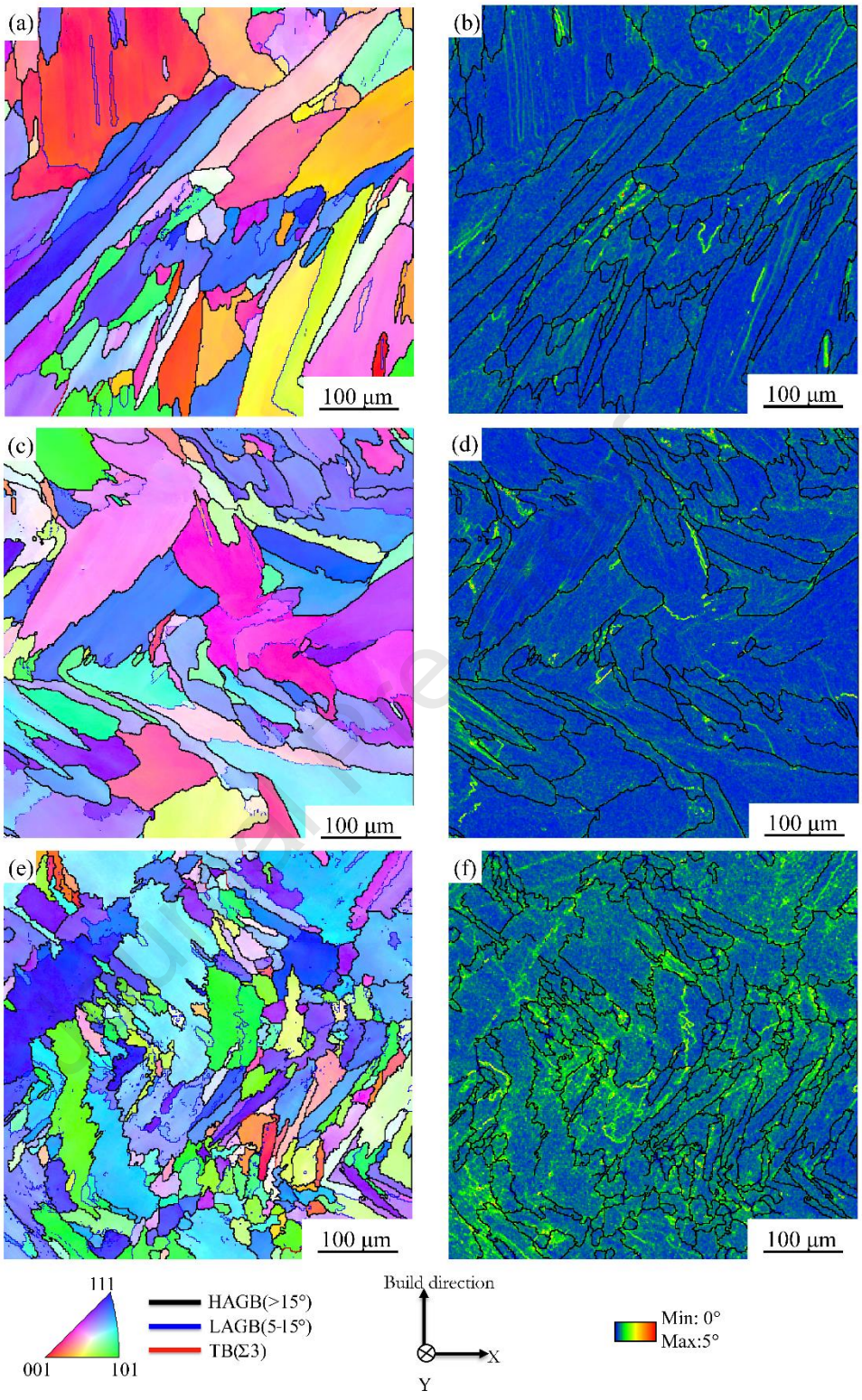

Fig.8 (a, c, e) IPF and **(b, d, f)** KAM maps of the **(a, b)** CoCrFeMnNi HEA fabricated with P=80 J/mm, **(c, d)** CoCrFeMnNi HEA fabricated with P=90 J/mm,

and **(e,f)** CoCrFeMnNi/TiB_2 composite fabricated with P=90 J/mm. The reference axis for the IPF map is the Z direction (i.e. build direction).

Fig. 8 gives the EBSD build-direction inverse pole figure (IPF) and the Kernel average misorientation (KAM) maps of the as-printed CoCrFeMnNi/TiB_2 specimen, together with those of the as-printed CoCrFeMnNi with P=80 J/mm and P=90 J/mm. The grain sizes of CoCrFeMnNi samples fabricated with the two linear energy inputs are determined to be 19 μm (P=80 J/mm) and 28 μm (P=90 J/mm), respectively. Higher energy input into the melt pool reduces the cooling rate, thereby coarsening the grains. In comparison, the CoCrFeMnNi/TiB_2 composite fabricated by 90 J/mm demonstrates the smallest grain size (13 μm). Such grain refinement phenomenon is mainly due to the high cooling rate and the increased number of grain nuclei sites via the addition of ceramic particles. The average radius of the heterogeneously formed nuclei decreases with ceramic particle size. Whereas, the critical undercooling required for the activation of solid transition (ΔT) is inversely proportional to the ceramic particle size [32]. Thus, the addition of small particles (i.e. below 2 μm in the casting process) may suffer from the risk of inadequate undercooling rate [2, 32], even though they are effective in grain refinement. During the laser deposition process, ΔT can be contributed by both constitutional supercooling (ΔT_c) and thermal supercooling (ΔT_t) [33, 34]. ΔT_t is profoundly enhanced due to the high cooling rate intrinsic to LENS, which guarantees the undercooling rate required and further contributes to more nucleation in the solidification front. Additionally, the enhanced cooling rate shortens the grain growth time compared to the CoCrFeMnNi by the same printing condition (P=90 J/mm).

TEM images (**Fig. 9**) show that TiB_2 reinforcements exist in the form of individual particles rather than agglomerated clusters. This may be attributed to the large thermal gradient in the melt pool, enhancing the radial circulating flow and the self-stirring effect of the liquid phase [14]. Furthermore, such separated reinforcements can provide more pronounced strengthening effects as compared with the agglomerated ones observed in conventionally processed MMCs. A high density of dislocations is

generated to accommodate the thermal mismatch originating from discrepancies of the thermal expansion and the elastic moduli between the dispersed particles and the matrix during printing.

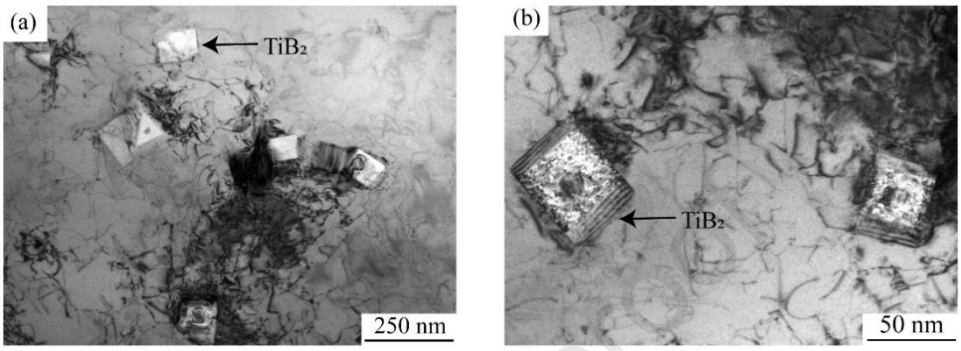

Fig .9 (a) Low and **(b)** high magnification of TEM images showing TiB_2 particles and dislocations in the as-deposited CoCrFeMnNi/TiB_2 composite.

.

3.3 Tensile properties and strengthening mechanisms

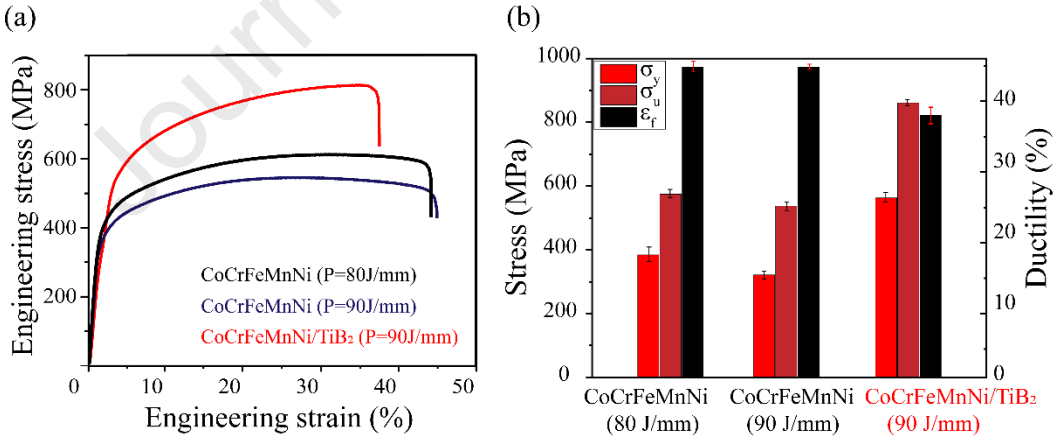

Fig. 10. (a) Engineering tensile stress-strain curves and **(b)** tensile properties summary of the as-deposited CoCrFeMnNi HEA (P= 80 J/mm; P= 90 J/mm) and CoCrFeMnNi/TiB_2 composite (P= 90 J/mm).

Fig. 10a exhibits the engineering tensile stress-strain curves of the as-printed CoCrFeMnNi/TiB_2 composite and CoCrFeMnNi HEA tested at ambient temperature. The extracted yield strength (σ_y), ultimate tensile strength (σ_u), and tensile strain (ε_f)

are summarized in **Fig. 10b**. Compared to the CoCrFeMnNi prepared under the optimized processing condition (P=80 J/mm), the addition of ceramic nanoparticles increases σ_y from 387 MPa to 567 MPa and the σ_u from 577 MPa to 861 MPa. The CoCrFeMnNi fabricated with P=90 J/mm shows a lower value of both σ_y (351 MPa) and σ_u (552 MPa). Even though the strength enhancement was achieved at the slight sacrifice of ductility, the average elongation to fracture (37%) of the composites still surpasses many reported CoCrFeMnNi HEAs in the absence of reinforcement [2, 4, 10].

For the as-printed CoCrFeMnNi, the yield strength ($\sigma_{Y\text{-}HEA}$) is related to (i) the instinct lattice friction stress (σ_0), (ii) the grain boundaries strengthening (σ_{GB}), and the dislocations strengthening (σ_{Dis}):

$$\sigma_{Y-HEA}=\sigma_0+\sigma_{GB}+\sigma_{Dis} \quad (2)$$

For the yield strength ($\sigma_{Y\text{-}HEA/TiB2}$) of as-deposited CoCrFeMnNi/TiB_2 composite, there also exists incremental contributions of dispersion strengthening (σ_D) and load-transfer effect strengthening (σ_L):

$$\sigma_{Y-HEA/TiB_2}=\sigma_0+\sigma_{GB}+\sigma_{Dis}+\sigma_D+\sigma_L \quad (3)$$

The analysis of the strengthening mechanisms has been illustrated in the Supplementary Information. The theoretical yield strengths are 362 MPa, 342 MPa and 570 MPa for CoCrFeMnNi (80 J/mm), CoCrFeMnNi (90 J/mm) and CoCrFeMnNi/TiB_2 composite (90 J/mm), respectively. The calculated values are close to the experimental results. **Fig. 11** clarifies the effects of each strengthening mechanism. It is discernible that dispersion strengthening accounts for 26.7% of the total yield strength, and is the most important reason for the improved yield strength of TiB_2/CoCrFeMnNi HEA composite. Meanwhile, the enhanced yield strengthen is also attributed to the refined grain sizes, increased dislocation density, and additional load transfer effect.

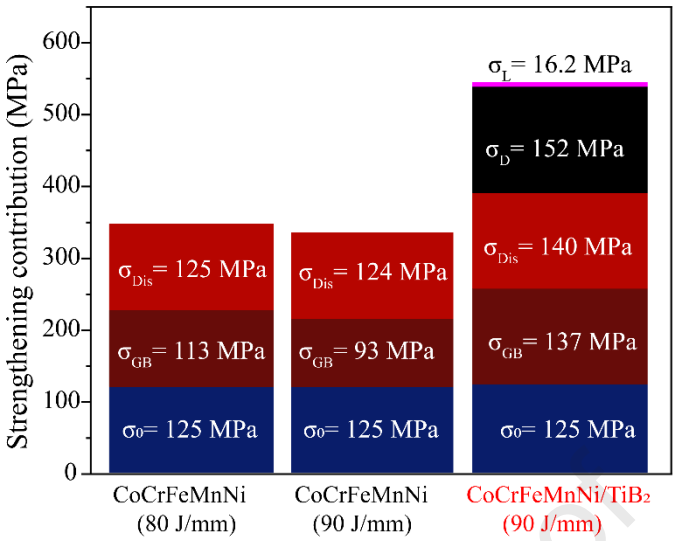

Fig. 11. Summary of contributions of different strengthening mechanisms.

3.4 Enhanced tribological properties

We also examined the tribological properties of the as-print CoCrFeMnNi and CoCrFeMnNi/TiB_2 composite. As the microhardness of the CoCrFeMnNi fabricated with 80 J/mm (191 HV) outperforms that with 90 J/mm (180 HV), the former is used to evaluate the advantages of TiB_2 addition. Accompanying the TiB_2 phases, the microhardness of the as-printed specimen increases to 275 HV, and the wear rate decreases from 3.42 mm^3/Nm to 1.48 mm^3/Nm. The 3D surface profiles observed by the Zygo microscope are displayed in **Fig. 12a and Fig. 12b**. The color difference demonstrates the depth variation of the worn surface. It also indicates that the CoCrFeMnNi specimen suffers more severe abrasive wear in the sliding duration. The cross-section profile of the wear tracks, as plotted in **Fig. 12c**, reveals the narrowed wear track of the CoCrFeMnNi/TiB_2 composite. Due to the repeated accumulation and elimination of wear debris, some fluctuations are observed in the curves of **Fig. 12c**. The maximum wear depth and an average width of CoCrFeMnNi reach 5.7 μm and 585 μm, respectively. Whereas, the corresponding values for as-printed CoCrFeMnNi/TiB_2 composite are 4.3 μm and 405 μm, respectively. The typical friction coefficient curves are presented in **Fig. 12d**. The average friction coefficient of CoCrFeMnNi/TiB_2 composite is 0.45, which is 22.4% lower than that of the CoCrFeMnNi (0.58).

The decrease in friction coefficient and wear rate is mainly attributed to the improved surface resistance via high-hardness TiB_2 addition. The oxides formed in the wear tracks also contribute to reducing the degree of wear. The BSE-EDS morphologies of the worn surface of CoCrFeMnNi/TiB_2 composite are given in **Fig. 13a-h**. These figures reveal that there are obvious tribo-oxide products on the worn surface. Characterized by low friction coefficient, the metal oxides are commonly known to be in-situ lubricants during the sliding wear [35, 36]. Besides, the TiB_2 particles can also serve as a self-lubricant component through serial oxidization from TiO_2, B_2O_3 to H_3BO_3, which was also reported in Ref. [35, 37].

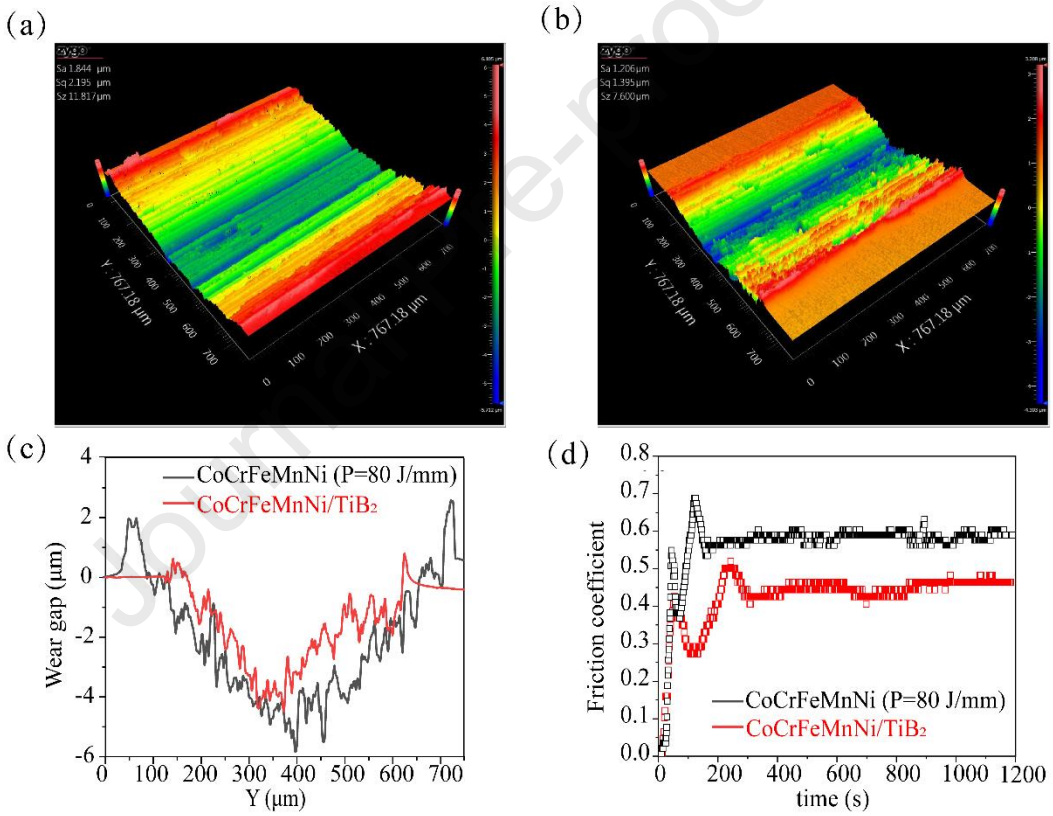

Fig. 12. 3D profiles of **(a)** CoCrFeMnNi (P=80 J/mm) and **(b)** CoCrFeMnNi/TiB_2 composite specimens (P=90 J/mm) after wear test; Cross-sectionl profile of **(c)** wear track and **(d)** friction coefficient of the specimens.

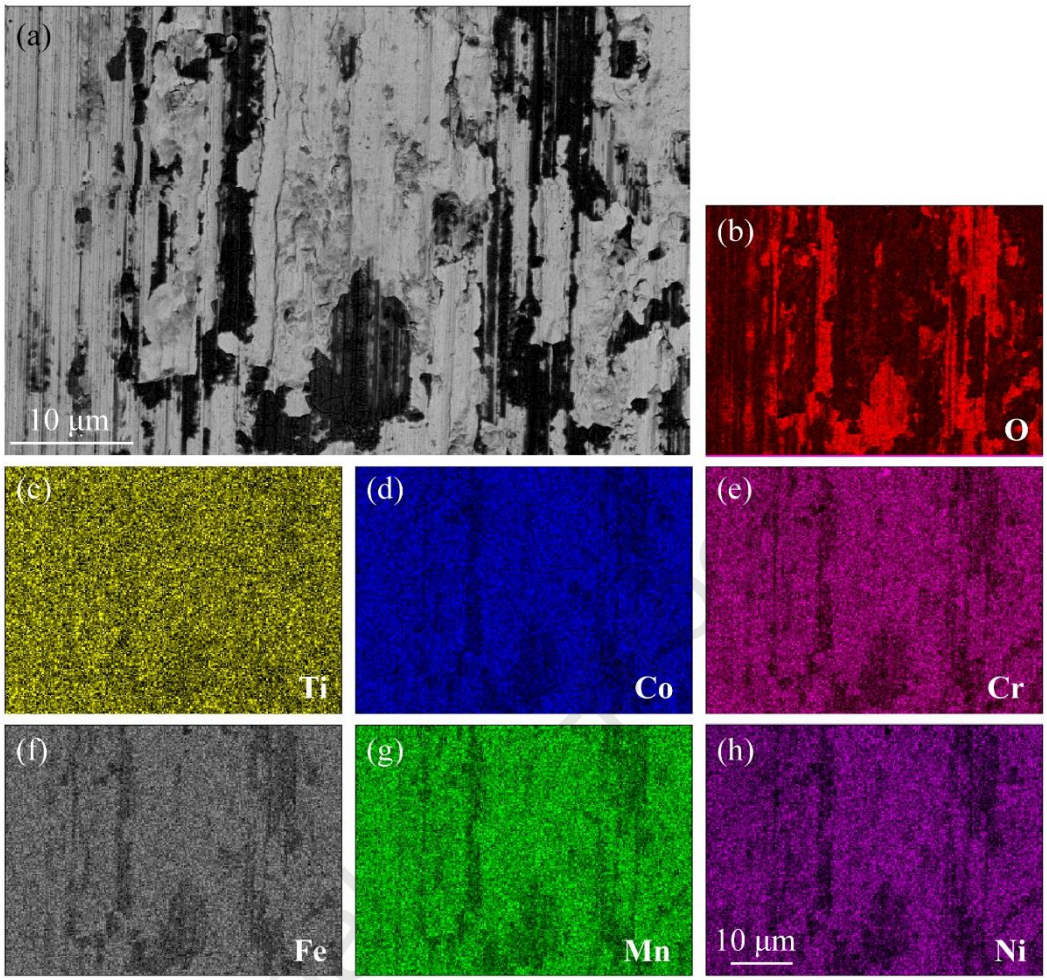

Fig. 13. **(a)** BSE and (**b-h)** EDS maps of the worn surface of the CoCrFeMnNi/TiB_2 composite (P=90 J/mm). The scale bar for (b-g) is the same as (h).

4. Conclusions

Near-fully dense TiB_2-reinforced CoCrFeMnNi HEA composites were successfully manufactured by LENS. Valuable insights were gained into understanding the effect of ceramic particle addition on the densification behavior, solidification behavior, as-printed microstructure, and tensile deformation behavior, and wear resistance in the TiB_2-reinforced CoCrFeMnNi HEA. The main conclusions drawn from this study are:

(1) The selected higher energy input for the LENS process of the composite reduced the viscosity of the melt and provided an enhanced self-stirring effect via Marangoni flow. Benefiting from the improved wettability between two components, the LENS-deposited CoCrFeMnNi/TiB_2 composite exhibited a high degree of densification of 99.72%, which was much higher than those of commonly reported MMCs.

(2) Under the combined effect of heterogeneous nucleation and altered thermal behavior during the printing process, grain-refined and dislocation-populated microstructures were formed in the CoCrFeMnNi/TiB_2 composite compared to the as-deposited CoCrFeMnNi.

(3) Different strengthening contributions during deformation at room temperature were quantitatively investigated, and the results show that the yield strengthening was predominantly attributed to dispersion strengthening, along with refined grain sizes, increased dislocation density, and additional load transfer effect.

(4) The wear resistance properties of CoCrFeMnNi/TiB_2 composite were superior to those of the CoCrFeMnNi due to the high hardness and self-lubrication of TiB_2.

Data availability

The raw/processed data required to reproduce these findings cannot be shared at this time as the data also forms part of an ongoing study.

Declaration of competing interest

The authors report no declaration of competing interest.

CRediT authorship contribution statement

Wang, Yilin: Conceptualization, Methodology, Data curation, Writing - original draft, Writing - review & editing. **Zhao, lei**: Writing - review & editing. **Wan,**

Di: Data curation, Writing - review & editing. **Guan, Shuai**: Writing - review & editing.

K.C. Chan: Supervision, Conceptualization, Writing - review & editing.

Acknowledgment

This work was financially supported by the Research Committee of The Hong Kong Polytechnic University under account no.G.45.56.R006.

References

[1] J.W. Yeh, S.K. Chen, S.J. Lin, J.Y. Gan, T.S. Chin, T.T. Shun, C.H. Tsau, S.Y. Chang, Nanostructured high-entropy alloys with multiple principal elements: novel alloy design concepts and outcomes, Adv. Eng. Mater. 6(5) (2004) 299-303.
[2] Z. Tong, X. Ren, J. Jiao, W. Zhou, Y. Ren, Y. Ye, E.A. Larson, J. Gu, Laser additive manufacturing of FeCrCoMnNi high-entropy alloy: Effect of heat treatment on microstructure, residual stress and mechanical property, J. Alloys Compd. 785 (2019) 1144-1159.
[3] F. Otto, A. Dlouhý, C. Somsen, H. Bei, G. Eggeler, E.P. George, The influences of temperature and microstructure on the tensile properties of a CoCrFeMnNi high-entropy alloy, Acta Mater. 61(15) (2013) 5743-5755.
[4] P. Chen, C. Yang, S. Li, M.M. Attallah, M. Yan, In-situ alloyed, oxide-dispersion-strengthened CoCrFeMnNi high entropy alloy fabricated via laser powder bed fusion, Materials & Design 194 (2020) 108966.
[5] H. Nami, A. Halvaee, H. Adgi, Transient liquid phase diffusion bonding of Al/Mg2Si metal matrix composite, Materials & Design 32(7) (2011) 3957-3965.
[6] D. Yim, P. Sathiyamoorthi, S.-J. Hong, H.S. Kim, Fabrication and mechanical properties of TiC reinforced CoCrFeMnNi high-entropy alloy composite by water atomization and spark plasma sintering, J. Alloys Compd. 781 (2019) 389-396.
[7] C. Salvo, E. Chicardi, C. García-Garrido, J.A. Jiménez, C. Aguilar, J. Usuba, R. Mangalaraja, The influence of mechanical activation process on the microstructure and mechanical properties of bulk Ti2AlN MAX phase obtained by reactive hot pressing, Ceram. Int. 45(14) (2019) 17793-17799.
[8] B. Song, Z. Wang, Q. Yan, Y. Zhang, J. Zhang, C. Cai, Q. Wei, Y. Shi, Integral method of preparation and fabrication of metal matrix composite: selective laser melting of in-situ nano/submicro-sized carbides reinforced iron matrix composites, Materials Science and Engineering: A 707 (2017) 478-487.
[9] Z. Zhao, J. Li, P. Bai, H. Qu, M. Liang, H. Liao, L. Wu, P. Huo, H. Liu, J. Zhang, Microstructure and mechanical properties of TiC-reinforced 316L stainless steel composites fabricated using selective laser melting, Metals 9(2) (2019) 267.

[10] A. Amar, J. Li, S. Xiang, X. Liu, Y. Zhou, G. Le, X. Wang, F. Qu, S. Ma, W. Dong, Additive manufacturing of high-strength CrMnFeCoNi-based High Entropy Alloys with TiC addition, Intermetallics 109 (2019) 162-166.
[11] J. Wang, H. Yang, Z. Liu, R. Li, J. Ruan, S. Ji, Synergistic effects of WC nanoparticles and MC nanoprecipitates on the mechanical and tribological properties of $Fe_{40}Mn_{40}Cr_{10}Co_{10}$ medium-entropy alloy, Journal of Materials Research and Technology 8(4) (2019) 3550-3564.
[12] B. Zhang, G. Bi, P. Wang, J. Bai, Y. Chew, M.S. Nai, Microstructure and mechanical properties of Inconel 625/nano-TiB_2 composite fabricated by LAAM, Materials & Design 111 (2016) 70-79.
[13] T. Wang, Y.Y. Zhu, S.Q. Zhang, H.B. Tang, H.M. Wang, Grain morphology evolution behavior of titanium alloy components during laser melting deposition additive manufacturing, Journal of Alloys and Compounds 632 (2015) 505-513.
[14] R. Shi, S.A. Khairallah, T.T. Roehling, T.W. Heo, J.T. McKeown, M.J. Matthews, Microstructural control in metal laser powder bed fusion additive manufacturing using laser beam shaping strategy, Acta Mater. 184 (2020) 284-305.
[15] C. Gao, W. Wu, J. Shi, Z. Xiao, A.H. Akbarzadeh, Simultaneous enhancement of strength, ductility, and hardness of TiN/AlSi10Mg nanocomposites via selective laser melting, Additive Manufacturing 34 (2020) 101378.
[16] B. AlMangour, Y. K. Kim, D. Grzesiak, K.-A. Lee, Novel TiB_2-reinforced 316L stainless steel nanocomposites with excellent room and high-temperature yield strength developed by additive manufacturing, Composites Part B: Engineering 156 (2019) 51-63.
[17] H. Wu, S. Huang, C. Zhao, H. Zhu, Z. Xie, C. Tu, X. Li, Microstructures and mechanical properties of in-situ FeCrNiCu high entropy alloy matrix composites reinforced with NbC particles, Intermetallics 127 (2020) 106983.
[18] B. AlMangour, D. Grzesiak, J. M. Yang, Nanocrystalline TiC-reinforced H13 steel matrix nanocomposites fabricated by selective laser melting, Materials & Design 96 (2016) 150-161.
[19] J. Zhang, B. Song, Q. Wei, D. Bourell, Y. Shi, A review of selective laser melting of aluminum alloys: Processing, microstructure, property and developing trends, Journal of Materials Science & Technology 35(2) (2019) 270-284.
[20] R. Unocic, J. DuPont, Process efficiency measurements in the laser engineered net shaping process, Metallurgical and materials transactions B 35(1) (2004) 143-152.
[21] L. Xi, D. Gu, S. Guo, R. Wang, K. Ding, K.G. Prashanth, Grain refinement in laser manufactured Al-based composites with TiB_2 ceramic, Journal of Materials Research and Technology 9(3) (2020) 2611-2622.
[22] D. Gu, H. Zhang, D. Dai, M. Xia, C. Hong, R. Poprawe, Laser additive manufacturing of nano-TiC reinforced Ni-based nanocomposites with tailored microstructure and performance, Composites Part B: Engineering 163 (2019) 585-597.
[23] B. Li, L. Zhang, Y. Xu, Z. Liu, B. Qian, F. Xuan, Selective laser melting of CoCrFeNiMn high entropy alloy powder modified with nano-TiN particles for additive manufacturing and strength enhancement: Process, particle behavior and effects, Powder Technol. 360 (2020) 509-521.

[24] G. Deng, A.K. Tieu, X. Lan, L. Su, L. Wang, Q. Zhu, H. Zhu, Effects of normal load and velocity on the dry sliding tribological behaviour of $CoCrFeNiMo_{0.2}$ high entropy alloy, Tribology International 144 (2020) 106116.
[25] C. Xie, S. Wu, Y. Yu, H. Zhang, Y. Hu, M. Zhang, G. Wang, Defect-correlated fatigue resistance of additively manufactured Al-$Mg_{4.5}$Mn alloy with in situ micro-rolling, J. Mater. Process. Technol. (2021) 117039.
[26] S. Guan, D. Wan, K. Solberg, F. Berto, T. Welo, T.M. Yue, K.C. Chan, Additive manufacturing of fine-grained and dislocation-populated CrMnFeCoNi high entropy alloy by laser engineered net shaping, Materials Science and Engineering: A 761 (2019) 138056.
[27] H. Li, Y. Huang, J. Sun, Y. Lu, The relationship between thermo-mechanical history, microstructure and mechanical properties in additively manufactured CoCrFeMnNi high entropy alloy, Journal of Materials Science & Technology 77 (2021) 187-195.
[28] A. Anal, T.K. Bandyopadhyay, K. Das, Synthesis and characterization of TiB_2-reinforced iron-based composites, J. Mater. Process. Technol. 172(1) (2006) 70-76.
[29] H. Yin, T. Emi, Marangoni flow at the gas/melt interface of steel, Metallurgical and Materials Transactions B 34(5) (2003) 483-493.
[30] A. Ostovari Moghaddam, N.A. Shaburova, M.N. Samodurova, A. Abdollahzadeh, E.A. Trofimov, Additive manufacturing of high entropy alloys: A practical review, Journal of Materials Science & Technology 77 (2021) 131-162.
[31] P. Chen, S. Li, Y. Zhou, M. Yan, M.M. Attallah, Fabricating CoCrFeMnNi high entropy alloy via selective laser melting in-situ alloying, Journal of Materials Science & Technology 43 (2020) 40-43.
[32] A.L. Greer, A.M. Bunn, A. Tronche, P.V. Evans, D.J. Bristow, Modelling of inoculation of metallic melts: application to grain refinement of aluminum by Al–Ti–B, Acta Mater. 48(11) (2000) 2823-2835.
[33] Q. Tan, J. Zhang, Q. Sun, Z. Fan, G. Li, Y. Yin, Y. Liu, M. X. Zhang, Inoculation treatment of an additively manufactured 2024 aluminium alloy with titanium nanoparticles, Acta Mater. 196 (2020) 1-16.
[34] J. Lelito, P.L. Zak, A.A. Shirzadi, A.L. Greer, W.K. Krajewski, J.S. Suchy, K. Haberl, P. Schumacher, Effect of SiC reinforcement particles on the grain density in a magnesium-based metal–matrix composite: Modelling and experiment, Acta Mater. 60(6-7) (2012) 2950-2958.
[35] X. Zhou, L. Jiang, S. Lei, W.Q. Tian, G. Wu, Micromechanism in self-lubrication of TiB2/Al composite, ACS applied materials & interfaces 7(23) (2015) 12688-12694.
[36] Z. Guo, A. Zhang, J. Han, J. Meng, Microstructure, mechanical and tribological properties of CoCrFeNiMn high entropy alloy matrix composites with addition of Cr3C2, Tribology International 151 (2020) 106436.
[37] F. Karpasand, A. Abbasi, M. Ardestani, Effect of amount of TiB_2 and B_4C particles on tribological behavior of Al7075/B_4C/TiB_2 mono and hybrid surface composites produced by friction stir processing, Surf. Coat. Technol. 390 (2020) 125680.

Highlights:

(1) Near fully dense 5 wt% TiB_2 nanoparticles containing CoCrFeMnNi high-entropy alloy matrix composites are fabricated via the laser engineered net shaping process.

(2) The ceramic reinforcements serve as nucleation sites and facilitate the formation of grain-refined and dislocation-populated microstructures.

(3) Ceramic addition can effectively enhance the tensile properties and wear resistance through a combination of mechanisms.

Figure captions

Fig. 1. SEM images of **(a)** CoCrFeMnNi HEA powders and **(b)** CoCrFeMnNi HEA/TiB_2 powders.

Fig. 2. The variation of the relative density with respect to the input linear energy density.

Fig. 3. Defect distributions for the CoCrFeMnNi/TiB_2 composite fabricated with *P*=90 J/mm. **(a-d)** are the corresponding high-resolution 3D X-ray CT micrograph of small regions chosen from the as-deposited **(a)** 1^{st}, **(b)** 3^{rd}, **(c)** 6^{th}, and **(d)** 10^{th} layer, respectively.

Fig. 4. The thermal maps of melt pool of **(a)** CoCrFeMnNi (80J/mm), **(b)** CoCrFeMnNi (90J/mm) and **(c)** CoCrFeMnNi/TiB_2 (90J/mm); **(d)** Temperature distribution (solid lines) and thermal gradient (dash lines) in the melt pool during printing. The melting point of CoCrFeMnNi (1613 K) is indicated by the bule broken line in (d).

Fig. 5. (a) Low and **(b-c)** high magnification SEM images of the as-printed CoCrFeMnNi/TiB_2 composites; **(d-i)** EDS mapping of the area in (a).

Fig. 6. XRD patterns of the as-deposited CoCrFeMnNi and CoCrFeMnNi/TiB_2 composite.

Fig .7. (a) OM and **(b)** SEM images of as-deposited CoCrFeMnNi/TiB_2 composite. The layer boundary and melt pool boundary are highlighted in red and white dashed lines, respectively.

Fig.8 (a, c, e) IPF and **(b, d, f)** KAM maps of the **(a, b)** CoCrFeMnNi HEA fabricated with P=80 J/mm, **(c, d)** CoCrFeMnNi HEA fabricated with P=90 J/mm, and **(e,f)** CoCrFeMnNi/TiB_2 composite fabricated with P=90 J/mm. The reference axis for the IPF map is the Z direction (i.e. build direction).

Fig .9 (a) Low and **(b)** high magnification of TEM images showing TiB_2 particles and dislocations in the as-deposited CoCrFeMnNi/TiB_2 composite.

Fig. 10. (a) Engineering tensile stress-strain curves and **(b)** tensile properties summary of the as-deposited CoCrFeMnNi HEA (P= 80 J/mm; P= 90 J/mm) and CoCrFeMnNi/TiB_2 composite (P= 90 J/mm).

Fig. 11. Summary of contributions of different strengthening mechanisms.

Fig. 12. 3D profiles of **(a)** CoCrFeMnNi (P=80 J/mm) and **(b)** CoCrFeMnNi/TiB_2 composite specimens (P=90 J/mm) after wear test; Cross-sectionl profile of **(c)** wear track and **(d)** friction coefficient of the specimens.

Fig. 13. **(a)** BSE and (**b-h)** EDS maps of the worn surface of the CoCrFeMnNi/TiB_2 composite (P=90 J/mm). The scale bar for (b-g) is the same as (h).

Declaration of interests

☒ The authors declare that they have no known competing financial interests or personal relationships that could have appeared to influence the work reported in this paper.

☐The authors declare the following financial interests/personal relationships which may be considered as potential competing interests: